Neohypoplasticity revisited

L. Mugele[*]; A. Niemunis[†]; H.H. Stutz[‡]

Abstract: This paper presents further improvements to the Neohypoplasticity, a constitutive model for sand, which overcomes some shortcomings of widely used hypoplastic models. The novelties presented in this paper includes a new description of the additional dilatancy due to the structural variable $\boldsymbol{z}$ and the introduction of a new state variable, denoted as $\boldsymbol{h}^r$, to consider the small strain stiffness in case of a 1D loading reversal. They remove shortcomings of earlier versions of Neohypoplasticity. The new formulations are presented and the performance of Neohypoplasticity is validated with experimental data from Karlsruhe fine sand. Both monotonic and cyclic tests are simulated under drained and undrained conditions. The results demonstrate that the Neohypoplasticity accurately reproduces the observed behaviour in monotonic and cyclic experiments.

Keywords: Neohypoplasticity, sand, element test, small strain stiffness

Notation and abbreviations

σ_{ij}	Cauchy stress (tension positive)
$R = \sqrt{\sigma_{ij}\sigma_{ij}}$	Euclidic norm of the stress tensor
$\mathring{\sigma}_{ij}$	Zaremba-Jaumann rate of the Cauchy stress
ε_{ij}	strain tensor (compression negative)
$\dot{\varepsilon}_{ij}$	strain rate
$p = -\sigma_{ii}/3$	Roscoe pressure
$q \overset{\text{triax}}{=} -\sigma_{11} + \sigma_{22}$	Roscoe deviatoric stress
$P \overset{\text{triax}}{=} -\sigma_{ii}/\sqrt{3}$	isometric pressure
$\|\boldsymbol{\sigma}^*\| = Q \overset{\text{triax}}{=} \sqrt{2/3}(-\sigma_{11} + \sigma_{22})$	isometric deviatoric stress
e	void ratio
z_{ij}	structural variable
h^r_{ij}	strain at the last reversal point
d^r	distance $\|\varepsilon_{ij} - h^r_{ij}\|$
E_{ijkl}	stiffness
C_{ijkl}	compliance
R_{ijkl}	rotational tensor
m_{ij}	hypoplastic flow rule
Y	degree of nonlinearity
$\sqcup^*$	deviatoric portion of $\sqcup$
$\| \sqcup \|$	Euclidean or Frobenius norm of $\sqcup$
$\vec{\sqcup} = \sqcup/\| \sqcup \|$	normalized $\sqcup$
δ_{ij}	Kronecker symbol
$\langle \sqcup \rangle$	Macaulay brackets
$I_{ijkl} = \frac{1}{2}\left(\delta_{ik}\delta_{jl} + \delta_{il}\delta_{jk}\right)$	symmetrizing identity tensor
$\langle \sqcup \rangle = 0.5(\sqcup + \| \sqcup \|)$	Macaulay brackets

---

[*]Researcher, Institute of Soil Mechanics and Rock Mechanics, Karlsruhe Institute of Technology, Germany (corresponding author). Email: luis.mugele@kit.edu

[†]Professor, Institute of Soil Mechanics and Rock Mechanics, Karlsruhe Institute of Technology, Germany

[‡]Professor, Institute of Soil Mechanics and Rock Mechanics, Karlsruhe Institute of Technology, Germany

HP	Hypoplasticity
NHP	Neohypoplasticity
IS	Intergranular strain
AFR	associated flow rule
CSL	critical state line
KFS	Karlsruhe fine sand

1 Introduction

The mechanical behaviour of sand is characterized by numerous nonlinear effects: barotropy and pyknotropy, dilatancy and contractancy, critical states as well as an increased stiffness due to a reversal of loading. In order to model such complex behaviour, hypoplastic constitutive models have been developed over the last decades [12]. Hypoplastic constitutive models, such as ones by Kolymbas [11], Wu [44], Bauer [2], Gudehus [8] and von Wolffersdorff [35] can be brought to the general rate form [16, 19]:

$$\mathring{\boldsymbol{\sigma}} = \mathsf{E} : \left(\dot{\boldsymbol{\varepsilon}} - f_d \boldsymbol{m} Y \|\dot{\boldsymbol{\varepsilon}}\| \right), \tag{1}$$

whereby $\mathring{\sigma}_{ij}$ is the Zaremba-Jaumann rate of the Cauchy stress and $\dot{\varepsilon}_{ij}$ describes the strain rate. The earlier form $\mathring{\boldsymbol{\sigma}} = \mathsf{L} : \dot{\boldsymbol{\varepsilon}} + \boldsymbol{N}\|\dot{\boldsymbol{\varepsilon}}\|$ of the Hypoplasticity used tensorial expressions for the second-order tensor N_{ij} as well as for the fourth-order tensor L_{ijkl} and is mathematically equivalent to (1) by setting $\mathsf{E} = \mathsf{L}$, the hypoplastic flow rule $\boldsymbol{m} = -(\mathsf{L}^{-1} : \boldsymbol{N})^{\rightarrow}$ and the degree of nonlinearity $Y = \|\mathsf{L}^{-1} : \boldsymbol{N}\|$ [16, 19]. Advantages of this particular framework of constitutive models, over classical elasto-plasticity, are:

- description of the dilatancy within the "yield surface"

- low stiffness for a "neutral load"

- realistic bifurcation (shear band)

- relatively straightforward implementation

A popular version of Hypoplasticity (HP) after von Wolffersdorf [35] was extended for cycles by the so-called Intergranular strain [23] (IS). An increased small strain stiffness was introduced after reversals. Thus, the so-called *ratcheting* was alleviated and cyclic deformations could be simulated without an excessive accumulation of the stress or strain. Complex problems such as vibratory pile driving [15, 30, 33], deep vibrocompaction [1, 18, 43], wave propagation [28, 29, 31] or gravitational energy storage [27] can be fairly well modelled using HP+IS.

However, the most widely used version HP+IS has several shortcomings, three of which are:

- The underestimation of the dilatancy effects in dense sand. The problem can be observed in simulations of a shallow foundation that leads to an unrealistic punching mechanism, see Figure 1a. In dense sand a so-called general shear failure is expected [34] instead of punching. The evolution of the void ratio is also unrealistic, see Figure 1a. Bulging next to the foundation cannot be reproduced even in very dense sand [34]. This is a serious deficit in a practically simple but important geotechnical problem.

- Element tests on a very dense sand show that monotonic shearing can surpass the condition $Y = 1.0$ (corresponds to the yield condition) reaching the tensile stress region. This follows from the definition of the degree of nonlinearity $f_d \cdot Y$ (Figure 2a). A purely isobaric shearing applied on dense sand can mobilize stresses beyond $\varphi^{\mathrm{mob}} = 90°$.
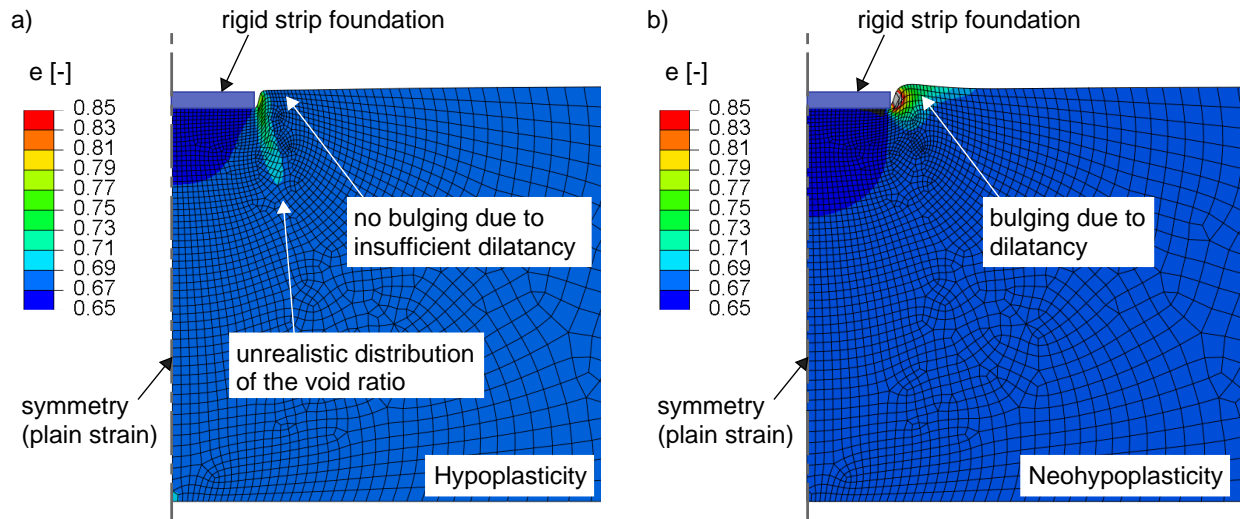
2

Figure 1: Simulation of a rigid strip foundation in dense sand: a) HP does not show a sufficient bulging of the surrounding soil due to insufficient dilatancy effects, whereby b) NHP overcomes the shortcomings.
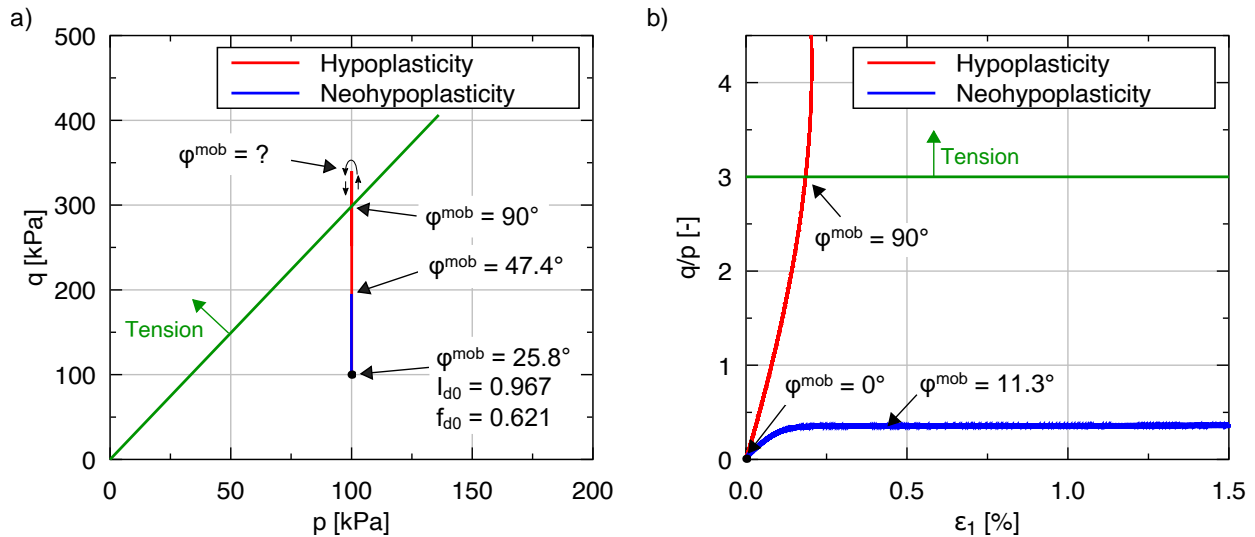

Figure 2: Element tests simulation show that HP and HP+IS (red curves) can surpass the tension limit: a) due to a monotonic shearing in dense sand and b) due to small cycles accompanied by a monotonic shearing. Using NHP (blue curves), these stress states are not possible in both cases.

- The IS increases the stiffness after reversals of the strain path direction, rendering the material response stiffer and more "elastic". If a monotonic shearing is superimposed by small cycling deformations, a tensile stress state can be reached due to this "elasticity" (Figure 2b).

The Neohypoplasticity (NHP) [21, 22] can overcome the above-mentioned shortcomings, see Figure 1 and Figure 2. The calculation of the rigid strip foundation is more realistic and tensile stresses are unachievable. Some further improvements to the version [21] are presented in this paper. The neohypoplastic equations are presented in detail in Section 2. The novel developments, which are presented in Section 2.6 and 2.8, are:

- an improved evolution equation of the structural variable $\boldsymbol{z}$

- a new definition of $\boldsymbol{m_z} = -\vec{\boldsymbol{\sigma}}$ instead of $\vec{\delta}_{ij}$ with emphasized deviatoric portion of the strain rate

3

- a simplified small strain stiffness formulation based on the *last strain reversal* $\boldsymbol{h}^r$ in place of the IS concept

To validate the model, laboratory tests on Karlsruhe fine sand (KFS) were simulated in Section 3. Triaxial and oedometric tests with monotonic and cyclic loading were simulated. Experimental data from the literature [36, 41] extended by some new experiments are used for comparisons. The results demonstrate that the NHP performs quite well. It was implemented into *Abaqus* as a user's material subroutine (*umat*). This implementation turned out to be a reliable tool for simulating the behaviour of granular materials. In Section 4, a comprehensive conclusion is given. An outlook and potential further developments of the NHP are proposed.

2 Neohypoplastic constitutive equations

The NHP was developed to overcome the disadvantages of the HP+IS mentioned in Section 1. The modified tensorial equation between the stress and the strain rate from the version of [21]

$$\mathring{\boldsymbol{\sigma}} = k \cdot \overline{\mathsf{E}} : \left(\dot{\boldsymbol{\varepsilon}} - \boldsymbol{m}Y\|\dot{\boldsymbol{\varepsilon}}\| - \omega\boldsymbol{m}^z\langle -\boldsymbol{z} : \dot{\boldsymbol{\varepsilon}}\rangle - \boldsymbol{m}^dY_d\|\dot{\boldsymbol{\varepsilon}}\| \right) \tag{2}$$

resembles roughly the shape of Eq. (1). The asymptotically hyperelastic stiffness $\overline{\mathsf{E}}$, the hypoplastic flow rule $\mathbf{m}$ and the degree of nonlinearity Y are redefined.

The state of soil is described by the effective stress $\boldsymbol{\sigma}$, the void ratio e and a tensorial structural variable $\boldsymbol{z}$. Moreover, a tensorial state variable called *last strain reversal* $\boldsymbol{h}^r$ was introduced in order take into account the small strain stiffness via a factor k. For the simulations of large cycles, the NHP includes a contractancy term $-\omega\boldsymbol{m}^z\langle -\boldsymbol{z} : \dot{\boldsymbol{\varepsilon}}\rangle$. An additional dilatancy term $\boldsymbol{m}^dY_d\|\dot{\boldsymbol{\varepsilon}}\|$ is addressed to avoid inadmissible dense states with $e < e_d(P)$. This problem was not considered in the most HP models [19]. The components of Eq. (2) are discussed in detail below. The improvements and modifications with respect to the version [21] are discussed in Section 2.6 and 2.8.

2.1 Hyperelastic stiffness

A purely hyperelastic constitutive response is expected upon small strains in soil. In this elastic regime, stress should be a $1-1$ function of strain $\boldsymbol{\sigma}(\boldsymbol{\varepsilon})$, which means that stress cannot be accumulated after any closed strain cycle. Apart from the constitutive model [6] the NHP is currently the only HP model for sand, which incorporates a hyperelastic stiffness, to the best knowledge of the authors. The hyperelastic stiffness E^* should guarantee (a) no accumulation of stress upon closed strain loops and (b) conservation of energy. Such stiffness can be derived from a complementary energy function

$$\bar{\psi}(\boldsymbol{\sigma}) = \sum_\alpha c_\alpha P^\alpha R^{2-n-\alpha} \quad \text{with} \quad \alpha \in \mathcal{R}. \tag{3}$$

with isometric stress invariants $P = -\sigma_{ii}/\sqrt{3}$ and $R = \sqrt{\sigma_{ij}\sigma_{ij}}$. A simple form of (3) with a single summand

$$\bar{\psi}(\boldsymbol{\sigma}) = cP^\alpha R^{2-n-\alpha}. \tag{4}$$

provides sufficient flexibility to represent the experimental data [10]. It must be noticed that for the determination of the material constants n, c, and α, extensive experimental investigations are required. For KFS, triaxial tests with local strain measurement were carried out [10]. A procedure to determine the material model parameters from the experimental data can be found in [13]. From the complementary energy function (4), the hyperelastic stiffness E^*_{ijkl} can be determined as the second partial derivative of ψ with respect to stress

$$\frac{\partial^2 \bar{\psi}}{\partial \sigma_{ij} \partial \sigma_{kl}} = C_{ijkl} = (E^*_{ijkl})^{-1} \tag{5}$$

It is also possible to determine n, c, α indirectly using the Poisson ratio ν and the degree of stress homogeneity n from the literature.

4

2.2 Rotation of the hyperelastic stiffness

Laboratory test [22, 36] have shown a difference in the maximum stress obliquity (i.e., the mobilized friction angle) in drained and undrained tests. This effect can be observed in both dense and loose samples. It cannot be attributed to shear banding [22] and can be described by a tensorial rotation of the hyperelastic stiffness E^* to $\overline{\mathsf{E}}$. This rotation depends on the current stress $\boldsymbol{\sigma}$, the void ratio e, and the structural variable $\boldsymbol{z}$, similar to the one used in the SaniSand model [3]. The evolution of $\boldsymbol{z}$ will be discussed in detail in the Section 2.6. In analogy to the Rodriguez formula, the operator R_{ijkl} is introduced for the rotation of the second-order stiffness tensors

$$R_{ijkl} = I_{ijkl} + (\cos\beta - 1)\left(u_{ij}u_{kl} + v_{ij}v_{kl}\right) - \sqrt{1 - (\cos\beta)^2}\left(u_{ij}v_{kl} - v_{ij}u_{kl}\right) \tag{6}$$

with the unit tensors $u_{ij} = -\vec{\delta}_{ij}$ and $v_{ij} = \vec{z}_{ij}$. The rotation angle β is given as a function of the current state of the soil by [21]

$$\beta = \left(\frac{\|\boldsymbol{z}\|}{z_{\max}}\right)^{n_L} \cdot \begin{cases} \beta_L \cdot \frac{e - e_c(P)}{e_i(P) - e_c(P)} & \text{for } e > e_c(P) \\ \beta_D \cdot \frac{e_c(P) - e}{e_c(P) - e_d(P)} & \text{for } e < e_c(P) \end{cases}. \tag{7}$$

The rotation angle β is positive and negative for loose and negative for dense sand respectively. The material parameters n_L, $\beta_L \geq 0$, $\beta_D \leq 0$, and z_{max} control the rotation of the stiffness. With two operators: extraction of the hydrostatic part $A_{ijkl} = \vec{\delta}_{ij}\vec{\delta}_{kl}$ and extraction of the deviatoric part $D_{ijkl} = I_{ijkl} - A_{ijkl}$, the modified stiffness can be expressed:

$$\overline{\mathsf{E}} = \mathsf{A} : \mathsf{E}^* + \mathcal{R} : \mathsf{D} : \mathsf{E}^* = (\mathsf{A} + \mathcal{R} : \mathsf{D}) : \mathsf{E}^*. \tag{8}$$

It is evident that only the deviatoric part of the material response is rotated. Isotropic compression and extension are not affected. The symmetry of the stiffness is lost, i.e. $\overline{E}_{ijkl} \neq \overline{E}_{klij}$. Consequently $\overline{\mathsf{E}}$ is not hyperelastic and the rotation can be interpreted as a nonlinearity. The stiffness $\overline{\mathsf{E}}$ becomes hyperelastic for $\beta = 0$. This is asymptotically reached for $\boldsymbol{z} = 0$ [20] (or in the critical state $e = e_c$). Therefore, a shakedown of the state variables caused by many closed strain cycles leads to a hyperelastic response.

The rotation of the stiffness is illustrated by response envelopes [7] in the P-Q diagram in Figure 3. In the triaxial compression region, shown in Figure 3a, an anticlockwise rotation is obtained for loose sand and a clockwise rotation for dense sand. In the triaxial extension region, shown in Figure 3b, the directions of the rotation is reversed. Different rotations for compression and extension regime can be seen for example in the stress paths of undrained triaxial tests. This behaviour is confirmed by experiments [20]. Note that the structural variable $\boldsymbol{z}$ in Figure 3 was initialized according to a monotonic strain path starting at $Q = 0$ towards the corresponding stress state in compression or extension.

2.3 Pressure dependent void ratios

The NHP uses the pressure dependent limit void ratios: e_d for the densest, e_i for the loosest and e_c for the critical one. The Bauer's compression curve [2] is used:

$$e_{\sqcup}(P) = e_{\sqcup 0} \exp\left[-\left(\sqrt{3}P/h_s\right)^{n_B}\right] \quad \text{with} \quad \sqcup = d, i, c \tag{9}$$

The material model parameters h_s and n_B need to be calibrated by curve fitting. The limiting void ratios e_{d0}, e_{c0}, e_{i0} can be estimated from laboratory tests [9].

2.4 Degree of nonlinearity

The degree of nonlinearity controls the "amount" of the anelastic behaviour and it is described as a joint function $Y(e, \boldsymbol{\sigma})$ of the stress and the void ratio and not as a product $f_d(e, P) \cdot Y(\boldsymbol{\sigma})$ used in older HP models [23, 35]. The stress invariant

$$H(\boldsymbol{\sigma}) = \operatorname{tr}\boldsymbol{\sigma}\operatorname{tr}\boldsymbol{\sigma}^{-1} - 9 \quad \in (0, \infty) \tag{10}$$

5
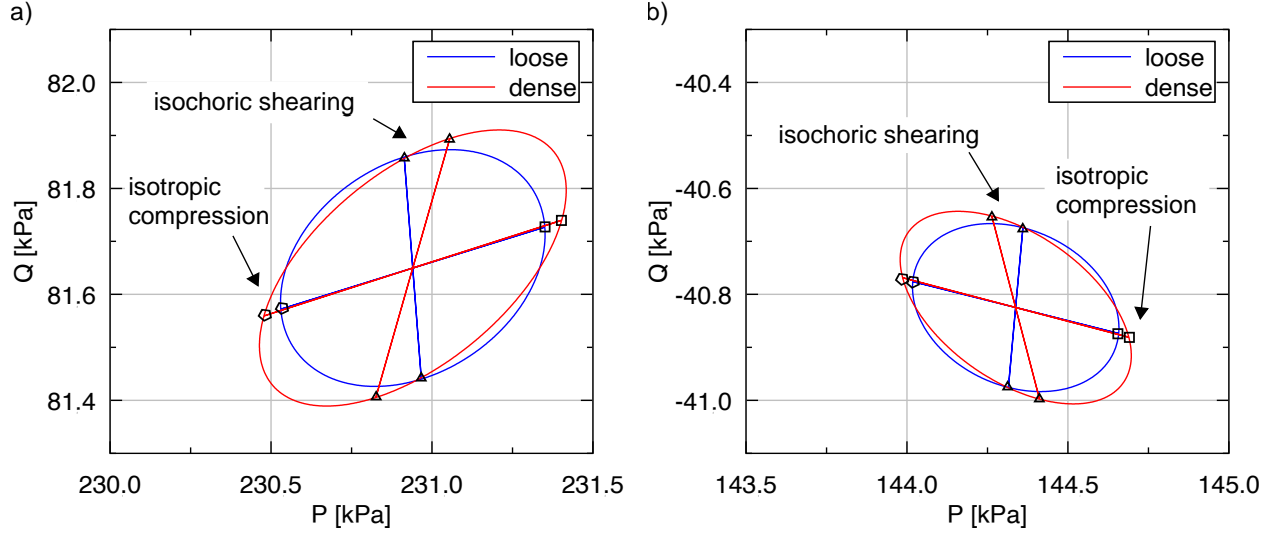
Figure 3: Response envelopes with predefined strain increments due to the elastic constitutive model $\mathring{\boldsymbol{\sigma}} = \overline{\mathsf{E}} : \boldsymbol{\varepsilon}$ (elastic part of NHP) in dense and loose sand: a) triaxial compression and b) triaxial extension.

is introduced for stresses in the negative octratant $\sigma_1 \leq \sigma_2 \leq \sigma_3 \leq 0$. The Matsuoka-Nakai criterium [17] can be written using $H(\boldsymbol{\sigma})$:

$$F_{M-N}(\boldsymbol{\sigma}) = H(\boldsymbol{\sigma}) - H_{\max} \leq 0 \quad \text{with} \quad H_{\max}(\varphi) = 8\tan^2[\varphi] \tag{11}$$

The pressure- and density-dependent peak friction angle φ is described as an empirical function

$$\varphi(e, P) = \varphi_c + \begin{cases} (\varphi_d - \varphi_c)\frac{e_c(P)-e}{e_c(P)-e_d(P)} & \text{for} \quad e < e_c(P) \\ (\varphi_c - \varphi_i)\frac{e-e_c(P)}{e_i(P)-e_c(P)} & \text{for} \quad e > e_c(P) \end{cases}, \tag{12}$$

whereby the critical friction angle φ_c, the friction angle at densest state φ_d and the friction angle at loosest state φ_i are material parameters. The degree of nonlinearity is:

$$Y(x) = A_Y \exp\left(-1/\left(B_Y x^{n_Y} + C_Y\right)\right) \quad \text{with} \quad x = \frac{H}{H_{\max}(\varphi)} \tag{13}$$

The material constants B_Y, C_Y and n_Y can be used for controlling the nonlinear term of both dense and loose sands, see Figure 4. The constant A_Y is not an independent one and it can be determined from the constraint $Y(1) = 1$. This condition is required for $\mathring{\boldsymbol{\sigma}} = 0$ for $\dot{\boldsymbol{\varepsilon}} \neq 0$ at the mobilized friction angle $\varphi(e, P)$ given in Eq. (12). It follows $A_Y = \exp(1/(B_Y + C_Y))$. The influence of the material model parameters B_Y, C_Y and n_Y on the degree of nonlinearity is also shown in Figure 4 and can be summarized:

- increase of B_Y enlarges the range with $Y \approx 1$

- increase of C_Y increase the minimum value $Y_{\min} = Y(0)$

- increase of n_Y enlarge the area where $Y \approx Y_{\min}$

2.5 Hypoplastic flow rule

The intensity of plastic strain is defined by the degree of nonlinearity $Y(e, \boldsymbol{\sigma})$ described in Section 2.4. The hypoplastic flow rule $\boldsymbol{m}$ (unit tensor) indicates the direction of the anelastic strain rate. It can be
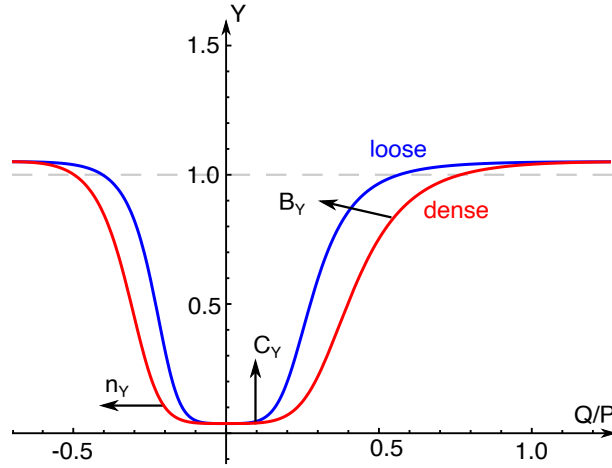
6

Figure 4: Influence of material constants B_Y, C_Y, n_Y and the void ratio on degree of nonlinearity $Y(e, \boldsymbol{\sigma})$ [21].

individually refined for different stress obliquities:

$$
m_{ij} = \begin{cases} m_{ij}^a = (\partial H/\partial \sigma_{ij})^{\rightarrow} = \left[\delta_{ij}\sigma_{kk}^{-1} - \sigma_{kk}\sigma_{ij}^{-2}\right]^{\rightarrow} & \text{for} \quad H \geq H_{\max}(\varphi_a) \\ m_{ij}^c = \left[\delta_{ij}\sigma_{kk}^{-1} - \sigma_{kk}\sigma_{ij}^{-2}\right]^{*\rightarrow} & \text{for} \quad H = H_{\max}(\varphi_c) \\ m_{ij}^i = (\delta_{ij})^{\rightarrow} & \text{for} \quad H = 0 \end{cases} \quad . \tag{14}
$$

with two interpolations:

$$
\begin{aligned} \boldsymbol{m} &= [x\boldsymbol{m}^c + (1-x)\boldsymbol{m}^i]^{\rightarrow} & \text{for} \quad & x = (H/H_{\max}(\varphi_c))^{n_1} \\ \boldsymbol{m} &= [x\boldsymbol{m}^a + (1-x)\boldsymbol{m}^c]^{\rightarrow} & \text{for} \quad & x = \left[(H - H_{\max}(\varphi_c))/(H_{\max}(\varphi_a) - H_{\max}(\varphi_c))\right]^{n_2} \end{aligned} \quad \text{or} \tag{15}
$$

The friction angle φ_a defines the stress ratio above which the associated flow rule (AFR) holds. In this case the AFR is simple the orthogonality $\boldsymbol{\sigma} : \boldsymbol{m} = 0$ and $\boldsymbol{m}^* \propto \boldsymbol{\sigma}^*$. According to Eq. (11) one can denote $\phi_a = \phi(\varphi_a)$. The interpolation with the exponents n_1 and n_2 provide further flexibility to model the hypoplastic flow rule at an arbitrary stress ratio. A schematic representation of the hypoplastic flow rule is given in Figure 5.
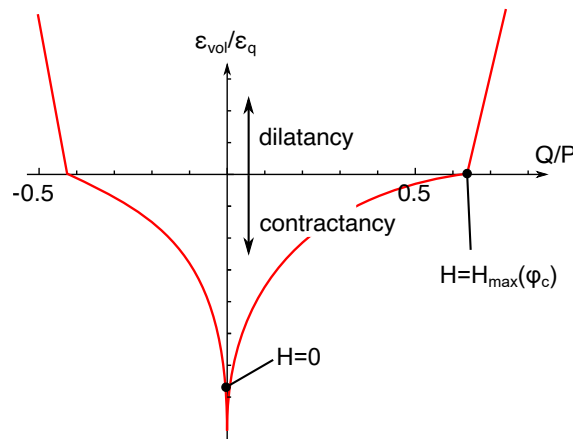

Figure 5: Hypoplastic flow rule $\boldsymbol{m}$ under triaxial conditions: dilatancy or contractancy as the ratio of volumetric strain ε_{vol} to deviatoric strain ε_q as a function of stress ratio Q/P.

2.6 Additional contractancy

A deviatoric state variable has been proposed by Dafalias et al. in the SaniSand model [3] and it can be interpreted as a mathematical description of the rolling of grains [21, 22]. From the micromechanical hypothesis in Figure 6, an individual grain can roll about a contact point with the neighbouring grain. It is possible during shearing at a large mobilised friction angle. This rolling is accompanied with negligible dissipation of energy, which corresponds to the AFR. Grains roll out on each other without frictional energy losses. The rolling back of the grains after a reversal of the loading direction leads to a strong contractancy. This contradicts the elastoplastic concept of elastic unloading (no contractancy). The additional contractancy is considered by the term $-\omega \boldsymbol{m}^z \langle -\boldsymbol{z} : \dot{\boldsymbol{\varepsilon}} \rangle$ in the NHP.
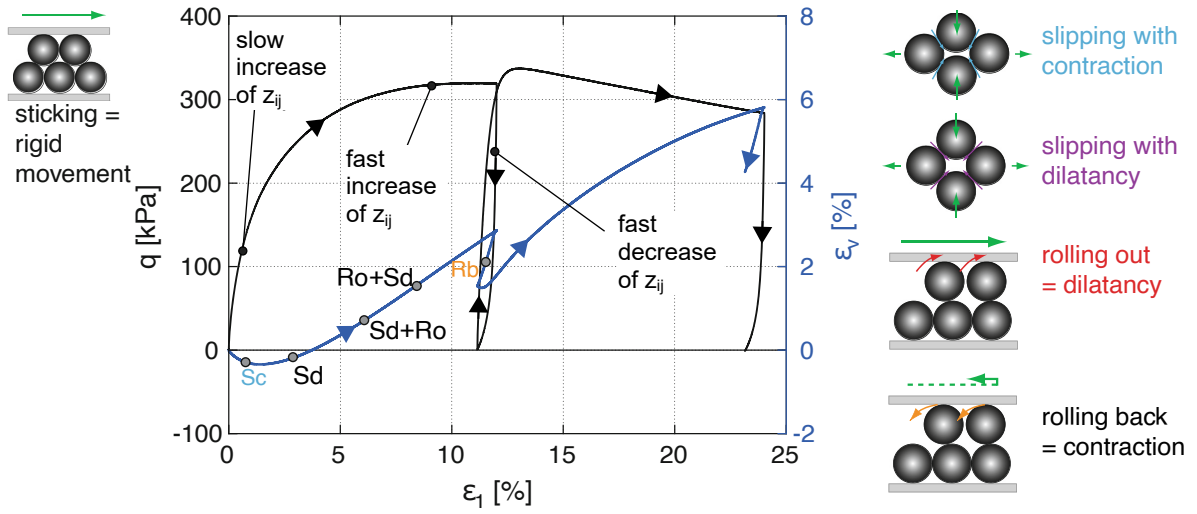

Figure 6: Micromechanical interpretation of drained triaxial shear deformation for different states on the conventional stress-strain-dilatancy diagram and the corresponding evolution of $\boldsymbol{z}$: slow increase at small deviatoric stress, fast increase at large deviatoric stress and fast decrease due to reversal of loading [21].

The structural variable z_{ij} has no volumetric part ($z_{ii} = 0$) and memorizes the recent history of the deviatoric strain. Beside the additional dilatancy, the structural variable $\boldsymbol{z}$ influences the rotation of the stiffness, as described in Section 2.2. The structural variable $\boldsymbol{z}$ develops due to monotonic shearing and its Euclidean norm asymptotically approaches the maximum value $z_{\max}$. A change in the direction of loading leads to a change in $\dot{z}_{ij}$. Generally:

- $\boldsymbol{z} : \dot{\boldsymbol{\varepsilon}} > 0$ holds for rolling out with dilatancy and
- $\boldsymbol{z} : \dot{\boldsymbol{\varepsilon}} < 0$ holds for rolling back with contractancy.

Due to the sign in the Macaulay brackets in the term $-\omega \boldsymbol{m}^z \langle -\boldsymbol{z} : \dot{\boldsymbol{\varepsilon}} \rangle$, only the contractancy term is taken into account in the NHP. The magnitude of the additional contractancy rate is defined as a pressure and density function $\omega(e, P)$ with the material constants $P_{\min}$, P_{ref}, $z_{\max}$ and k_d as:

$$\omega(e, P) = \omega^z(P) \cdot f_e(e) = \underbrace{\frac{P_{\text{ref}}}{z_{\max}(P_{\min} + P)}}_{\omega^z(P)} \cdot f_e(e) \tag{16}$$

with

$$f_e(e) = 1 - \frac{1}{1 + \exp(k_d(e - e_d))}. \tag{17}$$

8

The functions $\omega^z(P)$ and $f_e(e)$ and the influence of the material constants on these functions are shown in Figure 7. Figure 7a shows that the magnitude of the additional contractancy decreases with pressure and becomes negligible small at dense states via $f(e)$ (Figure 7b).
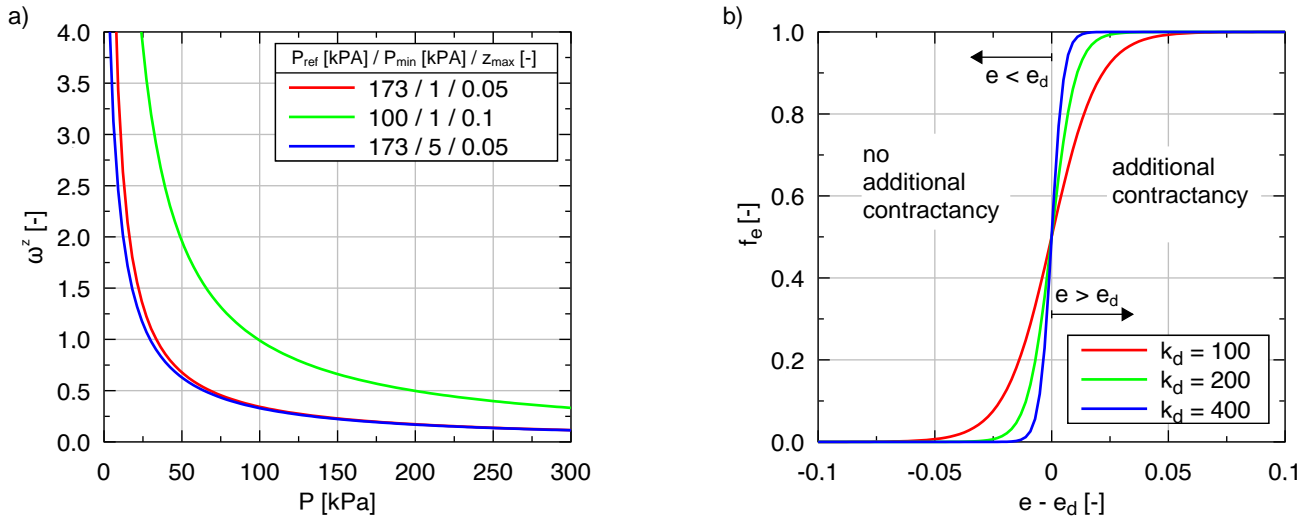

Figure 7: Additional dilatancy and its influence by material parameters: a) function $\omega^z(P)$ and b) function f_e.

Element tests reveal that in some cases $\omega^z(P)$ is too strong. Tensile stress states can be reached in the simulation if the function proposed in [21, 22] is used. Especially in the case of small mean effective stresses, the relaxation due to the additional contractancy can lead beyond the compression stress, for example, in the simulation of the so-called *butterfly effect*. Due to the pressure-dependent definition of ω, a highly pronounced additional contractancy occurs at small mean effective pressure, which dictates the stress relaxation in the direction of $\boldsymbol{m}^z$. The problem is shown in Figure 8a. In order to avoid results in unacceptable tensile stress states, the direction of the plastic deformations resulting from the additional contractancy is modified to the approach $\boldsymbol{m}^z = -\vec{\boldsymbol{\sigma}}$ (Figure 8a).
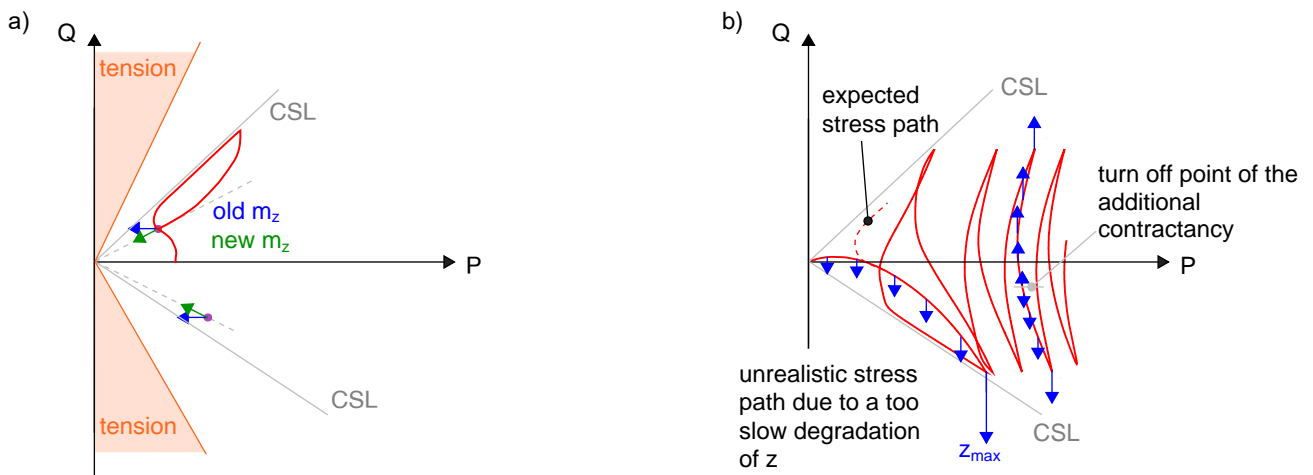

Figure 8: Problems in the simulation of the so-called butterfly effect: a) problematic direction of the additional contractancy m_{ij}^z and b) too slow decreasing of the structural variable z_{ij}.

The slow decay of $\boldsymbol{z}$ proposed in [21, 22] may lead to excessive relaxation after a load direction reversal (Figure 8b). Unrealistic stress paths can be observed at small effective stresses as the large additional

9

dilatancy at this stresses dictates the mechanical behaviour of the sand. Due to this problem, the *butterfly effect* cannot be reproduced. To address the described problem, a new evolution equation for $\boldsymbol{z}$ consists of three factors:

$$\dot{\boldsymbol{z}} = A_z \cdot \left(\dot{\boldsymbol{\varepsilon}}^{**} - \vec{\boldsymbol{z}} \left(\frac{||\boldsymbol{z}||}{z_{\max}} \right)^{\beta_z} ||\dot{\boldsymbol{\varepsilon}}^{**}|| \right) \left(\alpha_z + \left(\frac{||\boldsymbol{z}||}{z_{\max}} \right)^{n_z} \right), \tag{18}$$

With the strain rate $\dot{\boldsymbol{\varepsilon}}^{**}$ defined as

$$\dot{\boldsymbol{\varepsilon}}^{**} \stackrel{def}{=} \sin(\vartheta^r)^{20} \cdot \dot{\boldsymbol{\varepsilon}}^* = \left(\frac{\dot{\varepsilon}_Q^2}{\dot{\varepsilon}_Q^2 + \dot{\varepsilon}_P^2} \right)^{10} \cdot \dot{\boldsymbol{\varepsilon}}^* \qquad \text{with} \qquad \vartheta^r = \arctan\left(\frac{||\dot{\varepsilon}_Q||}{||\dot{\varepsilon}_P||} \right). \tag{19}$$

The angle ϑ^r describes the proportion between the deviatoric strain rate $\dot{\varepsilon}_Q$ and the volumetric strain rate $\dot{\varepsilon}_P$.

The volumetric strain rate slows the evolution of the structural variable $\boldsymbol{z}$. In the Eq. (27 old) from the version of [21] the structural variable $\boldsymbol{z}$ could accumulate also for K_0 compression, which seems to be incorrect. The factor $\sin(\vartheta^r)^{20}$ restricts the development of $\boldsymbol{z}$ to purely deviatoric strain rates, see Figure 9.
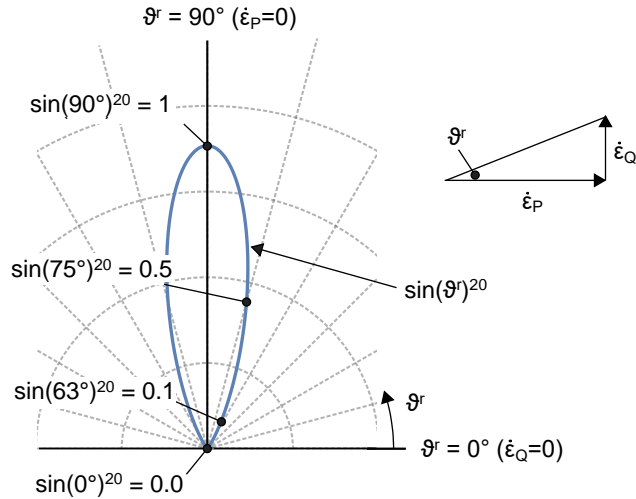

Figure 9: Function $\sin(\vartheta^r)^{20}$ as polar plot for the definition of the strain $\boldsymbol{\varepsilon}^{**}$, which develops the structural variable $\boldsymbol{z}$.

The evolution of $\boldsymbol{z}$ is parameterized with the constants α_z, n_z and β_z. The exponent β_z must be large enough to ensure a fast degradation even at low values of $\boldsymbol{z}$. The build up of $\boldsymbol{z}$ is faster for larger values of $\boldsymbol{z}$ but the asymptotic value $||\boldsymbol{z}|| = z_{\max}$ cannot be surpassed, i.e. $\dot{\boldsymbol{z}} = 0$ at $||\boldsymbol{z}|| = z_{\max}$ in Eq. (18). For this purpose, the entire rate of the evolution of $\boldsymbol{z}$ is scaled by $\left(\alpha_z + \left(\frac{||\boldsymbol{z}||}{z_{\max}} \right)^{n_z} \right)$. This positive feedback is achieved with the exponent $n_z = 2$. An evolution of $\boldsymbol{z}$ with small values of $\boldsymbol{z}$ is ensured by α_z, chosen to $\alpha_z = 0.01$.

Starting a triaxial unloading from $||\boldsymbol{z}|| = z_{\max}$ on the *critical state line* (CSL), $||\boldsymbol{z}|| = 0$ should reached due to shearing soon after Q vanishes. A too slow decay of $\boldsymbol{z}$ can lead to the problem presented in Figure 8b. In order to prevent this, the rate of evolution of $\boldsymbol{z}$ is scaled with the factor A_z. This factor must be calibrated with this objective. The calibration procedure can be found in the Appendix A.

2.7 Additional dilatancy for $e > e_d$

The pressure-dependent void ratio $e_d(P)$ describes the densest possible state of the soil. To avoid $e < e_d(P)$ an additional dilatancy term $\boldsymbol{m}^d Y_d ||\dot{\boldsymbol{\varepsilon}}||$ was introduced in Eq. (2) in [21] with $m_{ij}^d = \delta_{ij}$. The magnitude

of the additional dilatancy depends on the distance of the current state and the densest possible state

$$Y_d = f_{\text{ac}} \cdot Y_{\text{dd}} = f_{\text{ac}} \cdot \left(Y + 1 - (aP)^{1-n_B} \frac{(1 + e_d)}{\overline{E}_{PP} a n_B e_d} \right) \tag{20}$$

with

$$\overline{E}_{PP} = (\delta_{ij} E_{ijkl}) \delta_{kl} / \sqrt{3} \ \text{ and } \ a = \sqrt{3}/h_s. \tag{21}$$

The scalar factor

$$f_{\text{ac}} = 1 - \frac{1}{1 + \exp\left(k_d(e_d(P) - e)\right)} \tag{22}$$

is practically active only shortly before e approches e_d and is deactivated for states well above e_d. Details can be found in [20].

2.8   Small strain stiffness approach

The stiffness of the NHP from [21, 22] has been calibrated using monotonic tests with strains of about $\varepsilon \approx 10^{-3}$ [22]. The material parameter c of the hyperelastic potential function, see Section 2.1, is derived for this strains. An increased stiffness in the case of a loading reversal or generally a small strain stiffness has not been taken into account. However, especially for the simulation of cyclic deformations, the consideration of this small strain stiffness is indispensable.

Only 1D cycles will be applied and hence, instead of Paraelasticity [24, 25, 32], we propose a simplified approach increasing the stiffness after each load direction reversal. Overshooting due to a loading direction reversal in the case of $Y < 1$ should be expected.

First, a new tensorial state variable h_{ij}^r is introduced. It memorizes the strain at the last reversal of the strain path and is referred as the *last strain reversal*. A reversal is established when

$$(\varepsilon_{ij} - h_{ij}^r) : \dot{\varepsilon}_{ij} < 0 \tag{23}$$

occurs. The shortcomings of Eq. 23 are discussed in [24, 25, 32]. If the Eq. (23) is satisfied, the state variable h_{ij}^r is updated with the current strain $h_{ij}^r = \varepsilon_{ij}$. The previous last strain reversals are not memorized (contrarily to Paraelasticity [24, 25, 32]). The stiffness is proposed to be scaled

$$\overline{\mathsf{E}}^{\text{small}} = k \cdot \overline{\mathsf{E}} \qquad \text{with} \qquad k(d^r) = \left((m_R - 1)e^{(-\chi \cdot d^r)} + 1\right) \qquad \text{and} \qquad d^r \stackrel{def}{=} ||(\varepsilon_{ij} - h_{ij}^r)||. \tag{24}$$

The distance d^r from h_{ij}^r can only increase and k will gradually decreases from $k = m_R$ at $d^r = 0$ to $k = 1$ at $d^r = \infty$ decrease, see Figure 10. The material parameter m_R is the factor of the stiffness increase immediately after a reversal at $d^r = 0$. The constant χ controls the degradation of k due to a monotonic deformation and results from the assumed condition:

$$k(d^r = 10^{-3}) = m_R/2. \tag{25}$$

The proposed values are $m_R = 5$ and $\chi = 980$. A smaller range of stiffness increase can be achieved with a larger value of χ. Asymptotically $k = 1.0$ is reached with increasing d^r. The small strain stiffness can consequently be taken into account by a single material model parameter m_R modifying the factor k in Equation (2).
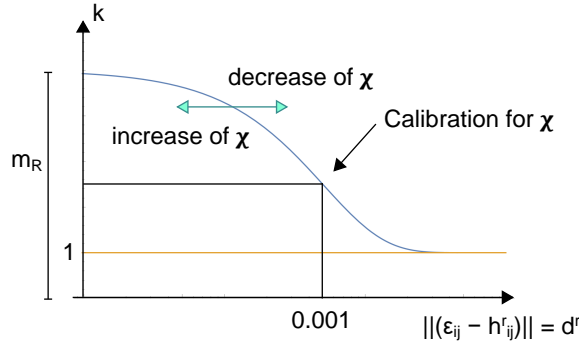
Figure 10: Increase factor k for the small strain stiffness approach.

3   Validation based on element tests

Oedometric and triaxial tests on Karlsruher Fine Sand (KFS) are simulated with the NHP. A large database of test results for this fine sand is available from [10, 36, 41, 42]. These test data were supplemented with several new laboratory tests on KFS conducted recently at KIT-IBF in the framework of this research. Widely used constitutive models such as Hypoplasticity with Intergranular strain [23, 35], the elastoplastic SaniSand model [3], and the Intergranular strain anisotropy (ISA) model [5] have already been used for simulations of the on KFS [4, 37, 41].

The KFS has a median particle size of $d_{50} = 0.14$ mm, a coefficient of uniformity of $C_u = d_{60}/d_{10} = 1.5$, a minimum void ratio of $e_{min} = 0.677$, and a maximum void ratio of $e_{max} = 1.054$. It is a quartz sand with a particle density of $\rho_s = 2.65$ g/cm^3 and sub-angular particle shape [36, 41].

NHP needs 28 material constants. The ones used here in the simulations of the experimental data for KFS are listed in Table 2. The numerical element test simulations were performed using the free available program code INCREMENTALDRIVER (www.soilmodels.com). The subroutine UMAT.FOR was written C. Grandas and A. Niemunis and modified in this research.

n [-]	c [-]	α [-]	h_s [kPa]	n_B [-]	e_{i0} [-]	e_{c0} [-]	e_{d0} [-]	φ_i[-]	φ_c[-]	φ_d[-]	φ_a[-]
0,6	0.001	0.1	$4 \cdot 10^6$	0.27	1.212	1.054	0.677	0.55850	0.57596	0.87267	0.87267

n_1 [-]	n_2 [-]	β_L [-]	β_D [-]	n_L [-]	B_Y [-]	C_Y [-]	n_Y [-]	z_{max} [-]	P_{min}[kPa]	P_{ref} [kPa]	k_d [-]
0.1	1	0.5	-0.2	1	20	0.3	2	0.05	1	$100\sqrt{3}$	200

a_z [-]	n_z[-]	β_z[-]	m_R[-]
0.01	2	0.2	5

Table 2: Parameter set of the NHP for KFS.

For calibration of different granular soils, we recommend to modify only 10 parameters: c, h_s, n_B, e_{i0}, e_{c0}, e_{d0}, φ_i, φ_c, φ_d, φ_a. One can distinguish between the well known material constants used in the HP h_s, n_B, e_{i0}, e_{c0}, e_{d0}, φ_c and the NHP-specific parameters c, φ_i, φ_d, φ_a, which should not be unnecessarily changed. Modifications of the remaining group of constants requires a higher expertise and are not recommended. The number of essential parameters is reduced by this from 28 to 10. The following comparisons between simulations and experimental data are presented the geotechnical sign convention (compression positive).

3.1   Oedometric test

Two oedometric compression tests with different initial relative densities are considered. The tests have been performed including one unloading and one reloading. The experimental test results (blue), which

are taken from [36, 41] and the numerical simulations (red) are shown in Figure 11. In the simulations, $z_{ij} = 0$ is initialized. The last strain reversal h_{ij}^r was initialised so that the stiffness at the start of the calculation is not increased. All simulations were started at the axial stress $\sigma_a = 1$ kPa. In addition to unloading to $\sigma_a = 1$ kPa (red), simulations with unloading of $\Delta\sigma_a = 250$ kPa (green) and $\Delta\sigma_a = 50$ kPa (black) were also conducted. In general, the NHP shows good agreement with the experimental data. The primary loading in the loose case is reproduced very well, see Figure 11a. Even in dense sand, the initial loading is well reproduced, only at high stresses the NHP shows a too-soft material behaviour, see Figure 11b. In all simulations, the increased stiffness is evident due to a load direction reversal. The simulations with small unloading steps show the so-called *overshooting*. This phenomenon is also known, from HP+IS. It should be mentioned that overshooting in NHP is only possible for stress states below the CSL, i.e. for $Y < 1.0$. In the case of $Y \approx 1.0$, no overshooting can occur in NHP, as shown in Section 3.3.
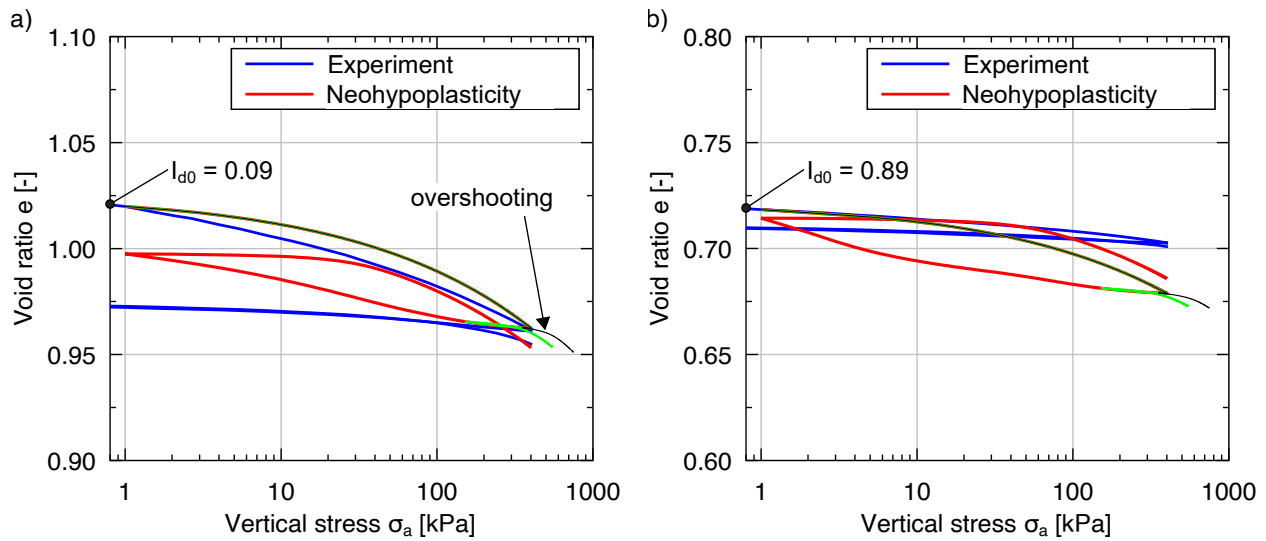

Figure 11: Oedometric compression tests on KFS: experimental results [36, 41] (blue) vs. calculations with NHP (red) a) loose sample and b) dense sample.

3.2 Monotonic triaxial tests

Figure 12 presents the results of monotonic, drained triaxial tests with different relative densities (blue) and the corresponding calculation results (red). The initial stress state were $p = 100$ kPa and $q = 0$ and the structural variable was initialized to $z_{ij} = 0$. The last strain reversal was set to $h_{ij}^r = 0$, i.e. the begin of shearing corresponds to a strain reversal point. The evolution of the deviatoric stress q is well reproduced by NHP, as shown in Figure 12a. The peak strength and the stiffness can be reproduced well. The development of volumetric strain is illustrated in Figure 12b and can be also accurately simulated. Recalculations of the same test using HP+IS can be found in [41, 36]. Compared to this simulations a better reproduction of the dilatancy in the NHP can be seen. These observations are consistent with the introductory example of the shallow foundation on dense sand. Both the initial contractancy and the subsequent dilatancy can be simulated. However, the transition from contractancy to dilatancy shows a small discrepancy between the experiments and simulations, resulting in a negligible defect.

Figures 13 and 14 present experimental results of monotonic triaxial tests under undrained conditions with different initial densities in the compression and extension case. Looser samples exhibit a more pronounced contractancy, which leads to a reduction of the effective stresses in the sample. To represent the initial experimentally observed contractancy, the structure variable was initialised to $||z_{ij}|| = z_{zmax}$ (solid line). A complete mobilisation in the opposite direction to the simulated triaxial compression was
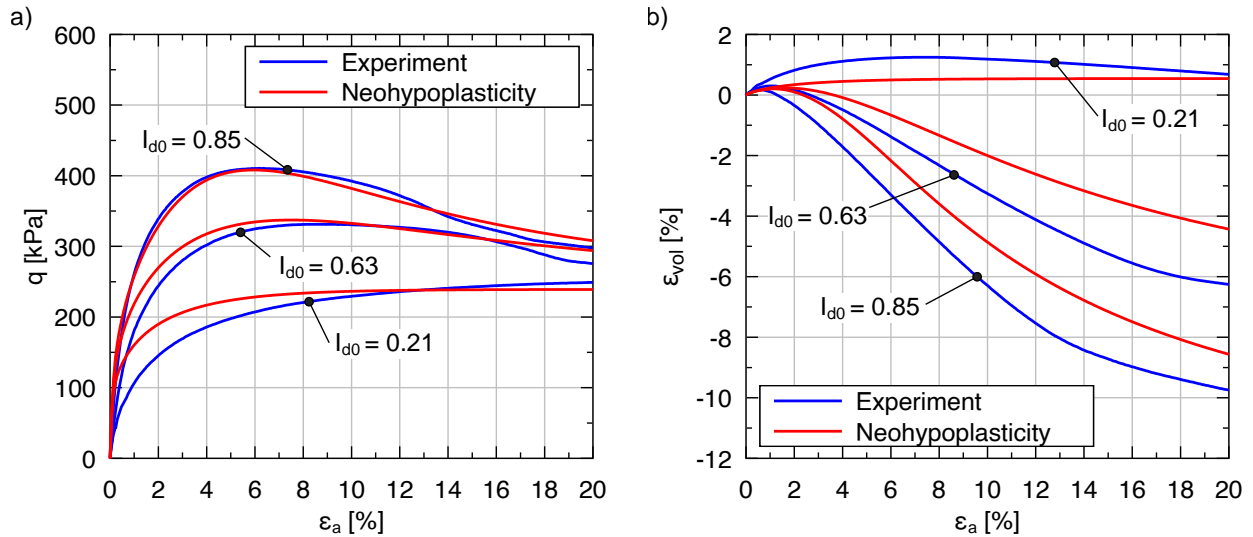
13

Figure 12: Monotonic, drained triaxial tests on KFS with three different initial densities: experimental results [36, 41] (blue) vs. calculations with NHP (red): a) evolution of the deviatoric stress q and b) volumetric strain ε_{vol} as a function of axial strain ε_a.

assumed. It is assumed that the sample preparation already creates a structure in the sample, which can be taken into account by initialising the structural variable $\boldsymbol{z}$ and which cannot be disturbed by the isotropic compression, Eq. 18. The dashed lines, in contrast, represent an initialisation of $z_{ij} = 0$. A smaller relaxation of the mean effective pressure occur. The last strain reversal was initialised to $h_{ij}^r = 0$. After the so-called *phase transformation* is reached, an increase in mean effective stress can be observed due to dilatancy. This behaviour can be seen in the test results (blue) in the *p-q* diagram, shown in Figure 13a) and 14a). The phase transformation can also be observed in the evolution of the deviatoric stress, shown in Figure 13b and 14b, by local minima. It is found that the NHP can qualitatively reproduce the mechanical behaviour under undrained conditions.
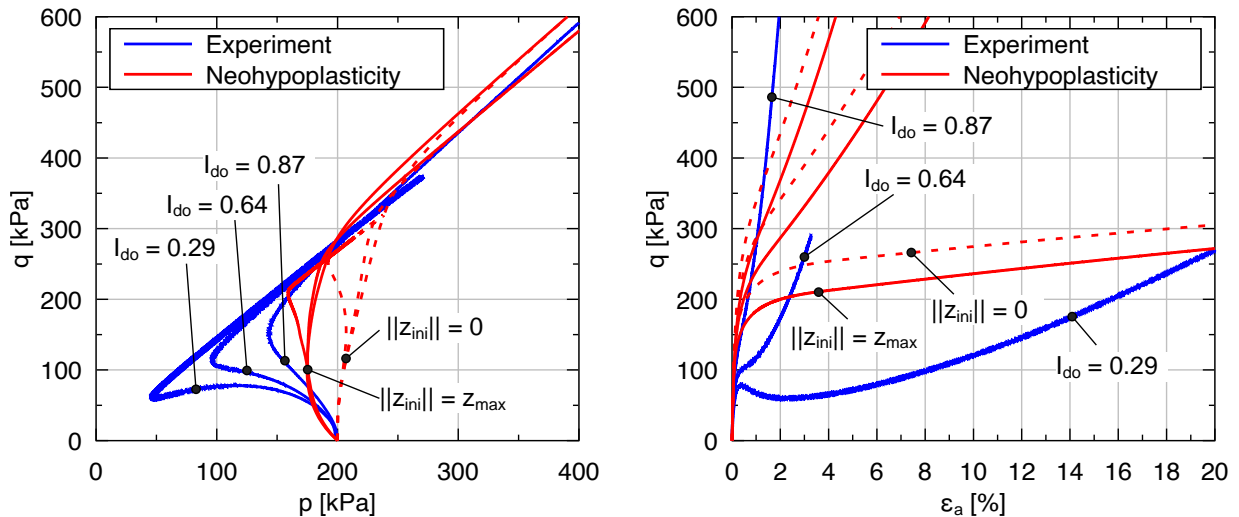

Figure 13: Monotonic, undrained triaxial compression tests on KFS with three different initial densities: Experimental results [36, 41] (blue) vs. calculations with NHP (red): a) stress path in $p - q$ diagram and b) evolution of deviator stress q as a function of axial strain ε_a.
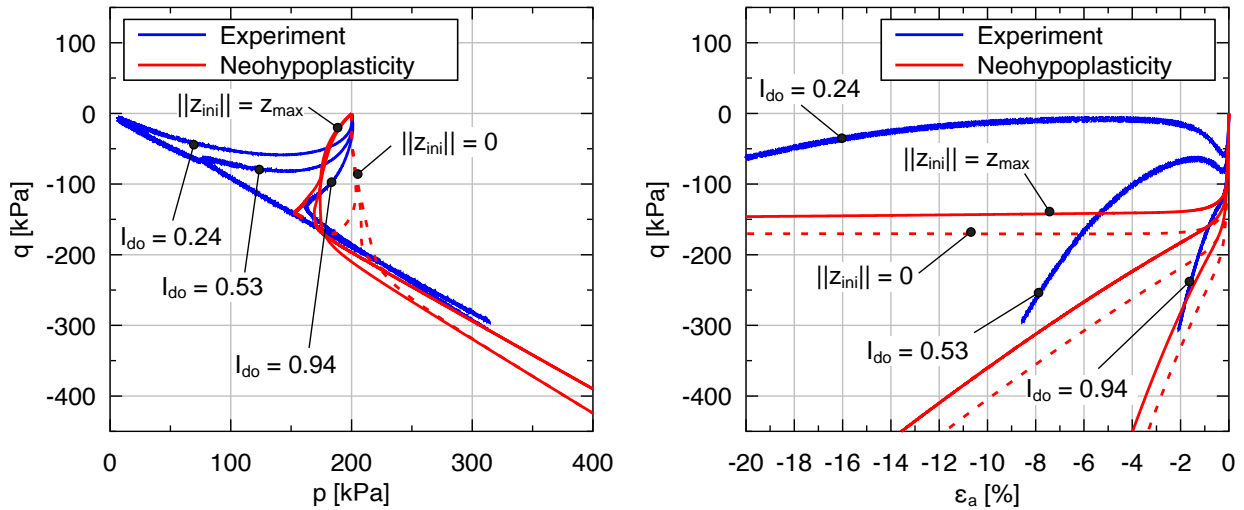
14

Figure 14: The same as Figure 13, but for triaxial extension test.

3.3 Triaxial tests with loading reversal

A monotonic, drained triaxial compression test with a medium initial density is considered, in which the sample was loaded to a strain of $\Delta\varepsilon_1 = 6$ %, then unloaded to $q = 0$, and subsequently reloaded [36]. The test clearly shows the different stiffness of sand due to loading, unloading, and reloading, see Figure 15. NHP can qualitatively reproduce this different stiffness. Although the experimentally observed stiffness due to reloading is greater than the predicted stiffness from NHP, see Figure 15a. Some advanced constitutive models exhibit an overshooting when similar tests are subjected to small unloading. This overshooting refers to a substantial overestimation of the experimental stress path resulting from a small unloading and subsequent reloading. To examine whether NHP is affected by overshooting, an additional numerical test with unloading steps of $\Delta q = 100$ kPa was simulated, see green curve in Figure 15. NHP does not exhibit overshooting in this case even if the simulated stiffness is underestimated upon reloading. As already mentioned before, despite the considered small strain stiffness, no overshooting will occur in the case of $Y = 1.0$ in NHP. This is because of the explicit formulation of the degree of nonlinearity, which is independent of the stiffness. As a result, the shear strength of NHP cannot be overestimated due to the small strain stiffness, which is essential in the context of a reliable design of structural elements. For comparison, HP+IS would lead to a significant overestimation of the deviator stress and corresponding to the strength in the same case [4]. The evolution of the volumetric strain is only qualitatively reproduced, as shown in Figure 15b. The contractancy due to a reversal of the direction of load is represented, however, the dilatancy is slightly underestimated.

In the following, the effectiveness of NHP in modelling the soil behaviour due to cyclic loading is demonstrated. The experimental and simulation results of a cyclic triaxial test under drained conditions are presented in Figure 16. The experiments were conducted at the Karlsruhe Institute of Technology and involved applying a cyclic load of $\Delta q = 50$ and $\Delta q = 60$ kPa. The tests were conducted on loose and isotropically consolidated samples with $I_d \approx 0.4$ and $p_0 = 100$ kPa. Compared to experiments from [36], a large amplitude-pressure ratio of $\zeta = q^{\mathrm{ampl}}/p^{\mathrm{av}} = 0.5$ respectively $\zeta = 0.6$ results. The cumulative compaction as a function of the number of cycles is shown in 16. The experiments reveal a highly pronounced densification within the first cycles. However, the accumulation rate decreases significantly with increasing number of cycles. This observation corresponds in general with experimental investigations, which were carried out, for example, in the context of the development of the HCA model [26, 36].

NHP can reproduce the experimental data very well. First of all, the resulting densification as a result of the cyclic deformation can be modelled. NHP enables a calculation of 5000 cycles with a realistic compaction rate, even after 5000 cycles. Especially at a stress amplitude of $\Delta q = 60$ kPa the accumula-
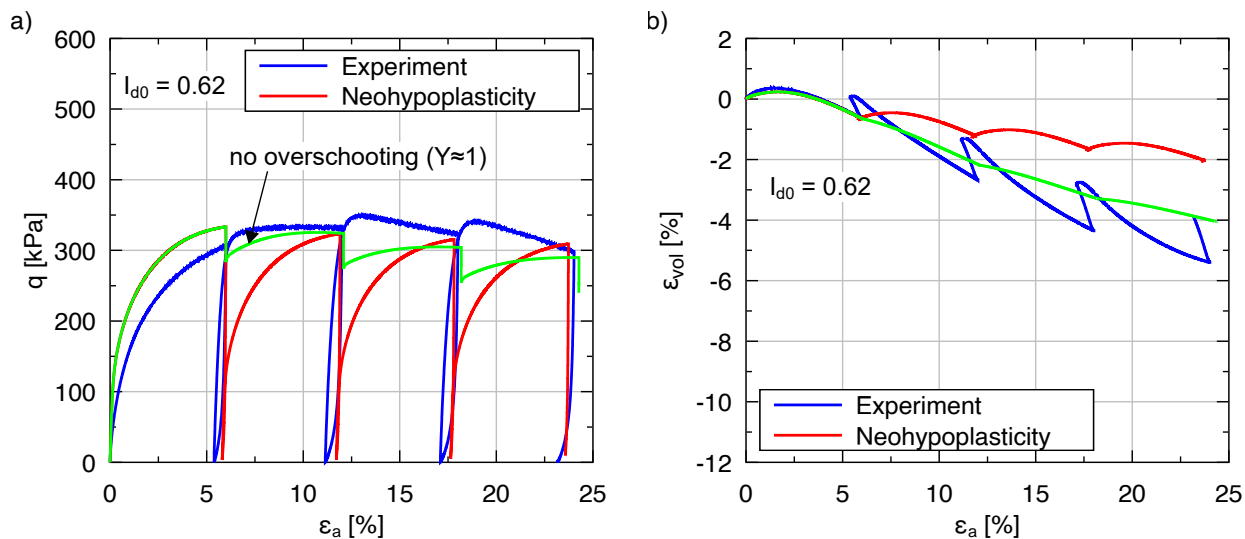
15

Figure 15: Monotonic, drained triaxial test on KFS with four unloading and three reloading steps on a sample with medium dense initial density: experimental results [36, 41] (blue) vs. calculations with NHP (red): a) evolution of the deviator stress q and b) volumetric strain ε_{vol} as a function of the axial strain ε_a. The green curve presents the calculation for a smaller stress unloading by $\Delta q = 100$ kPa.

tion rate is almost exactly achieved. For a stress amplitude of $\Delta q = 50$ kPa, a larger deviation appears. However, for an implicit constitutive model, this accumulation simulation is also quite reliable. For comparison: HP+IS would already predict the densest state after a few 100 cycles. In the experiment as well as in the simulations using NHP, this state is not reached even after 5000 cycles. It should be noted that the experimentally observed decrease of the accumulation rate with the number of cycles cannot be reproduced sufficiently accurately by NHP, since a state variable, which is required for this purpose does currently not exist. In general, the accumulation can be calibrated by the degree of nonlinearity Y especially through the parameter C_Y.
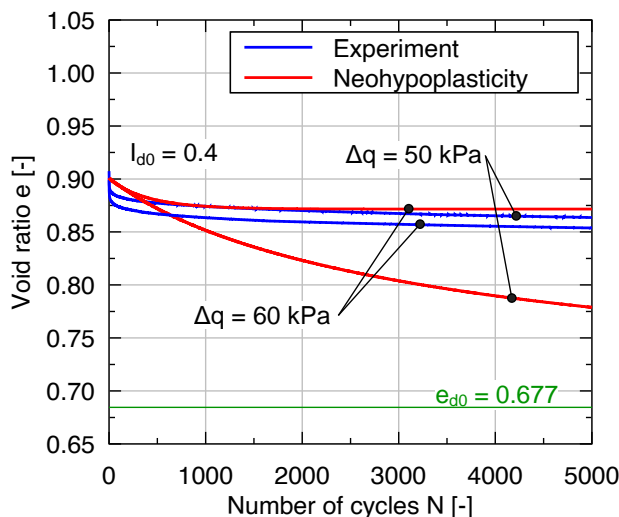

Figure 16: Cyclic drained triaxial test with large amplitude of the deviator stress: evolution of the void ratio e as a function of the number of cycles N for the experiments (blue) and the simulations with NHP (red).

Finally, cyclic undrained triaxial tests were considered [36, 41]. The results are presented for an isotropic consolidated sample with stress cycles in Figure 17. Figure 18 shows a test with predefined stress cycles, but with an anisotropic consolidation. Finally, an anisotropic consolidated sample with strain cycles is

16

shown in Figure 19.

The experiments demonstrated a progressive decrease in effective stress due to a hindered contractancy (relaxation), as depicted in Figure 17a, 18 a) and 19a). When the stress path reaches the critical state line (CSL) in the tests with stress cycles, large deformations occur. In the isotropically consolidated test a butterfly-shaped pattern, known as the butterfly effect, is exhibited, see Figure 17a. The axial strains required to accommodate the given deviator stress are larger in the extension region than in the compression region, as shown in Figure 17b. The simulation of the anisotropic consolidated test with stress cycles is also reproduced well.

In an undrained cyclic triaxial test with predefined strain cycles, soil liquefaction defined by $p = q = 0$ is experimentally achieved. Also, this phenomena can be modeled by NHP, see Figure 19a. Finally, it should be noted that the stiffness, which is represented by the inclination in the $q - \varepsilon_1$-diagram, can be represented in the three considered undrained triaxial tests with a very good approximation.
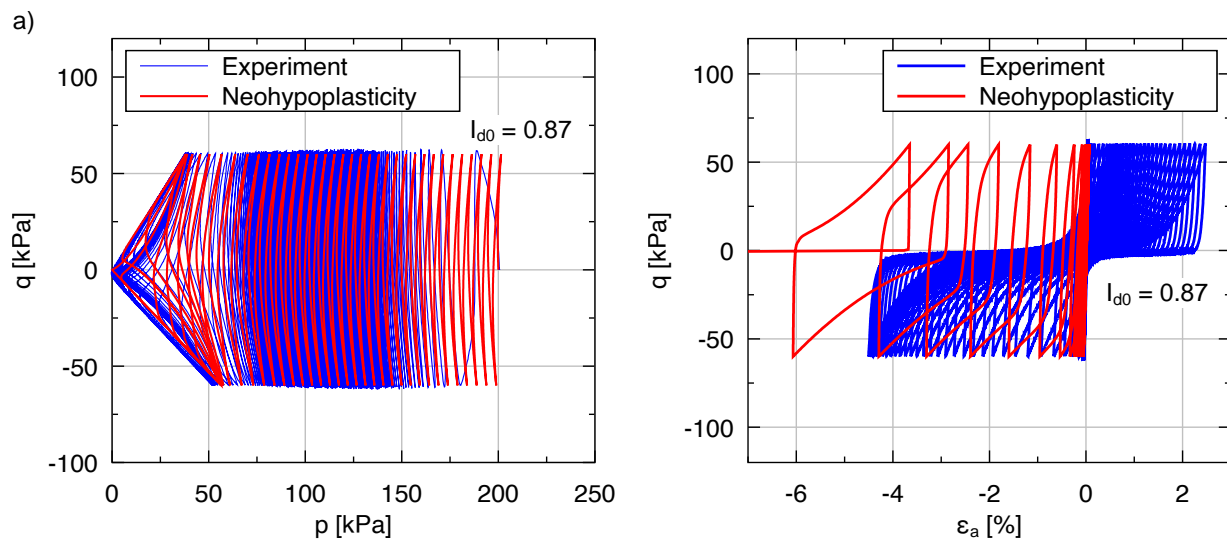

Figure 17: Isotopic consolidated cyclic undrained triaxial test with a stress amplitude of $\Delta q = 50$ kPa: experimental results [36, 41] vs. calculations with NHP: a) stress path in $p - q$ diagram and b) deviator stress q as a function of axial strain ε_a.

3.4 Investigation of the small strain stiffness

Especially the representation of the increased stiffness at small strains associated with it the degradation of shear modulus with increasing shear strain amplitude and a simultaneous increase of the damping ratio is a novel feature of NHP, see Section 2.8. Experimental data for the increased stiffness at small shear strain amplitudes can be found in the literature [36, 38, 39, 40].

Figure 20 represents the shear modulus determined from simple shear tests as a function of shear strain amplitude and the corresponding damping ratio using NHP with the novel small strain stiffness approach. Cyclic simple shear tests (with constant vertical stress) on a loose and a dense sample were considered. The stiffness was determined in the fifth cycle. The red lines correspond to the simulation using NHP and the blue area presents the corresponding expected area for natural sand. It becomes evident that the implemented small strain stiffness performs well and can reproduce the experimentally observed soil behaviour. However, it must be mentioned that reversals of 180° were simulated. It must be expected that only small changes in the shear direction cannot be adequately reproduced with the simplified approach.
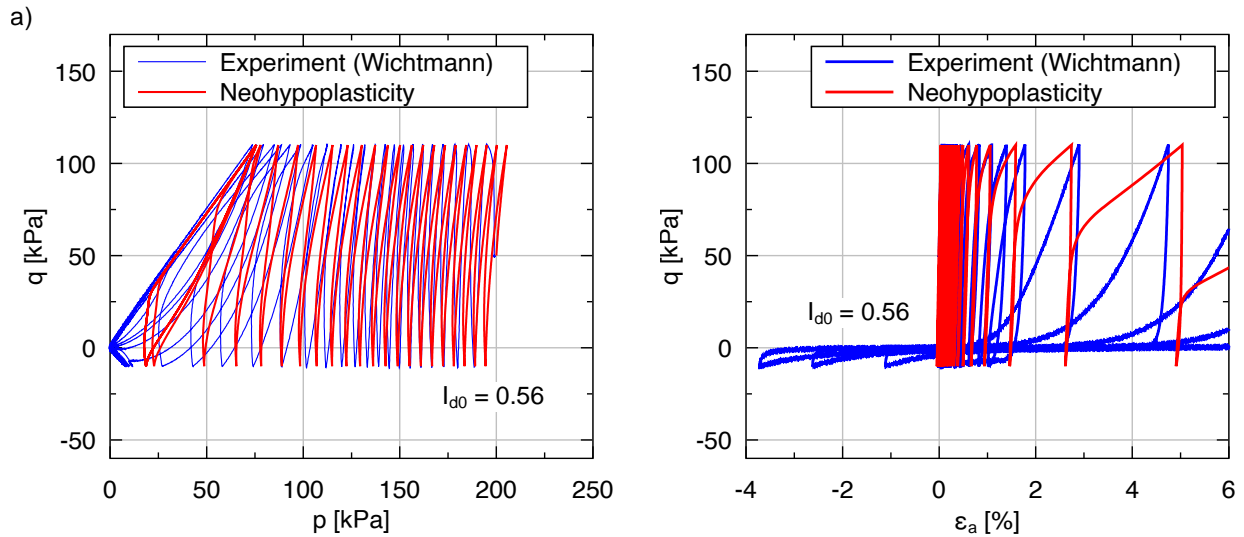
17

Figure 18: Anisotropic consolidated cyclic undrained triaxial test with a stress amplitude of $\Delta q = 60$ kPa: experimental results [36, 41] vs. calculations with NHP: a) stress path in $p - q$ diagram and b) deviator stress q as a function of axial strain ε_a.
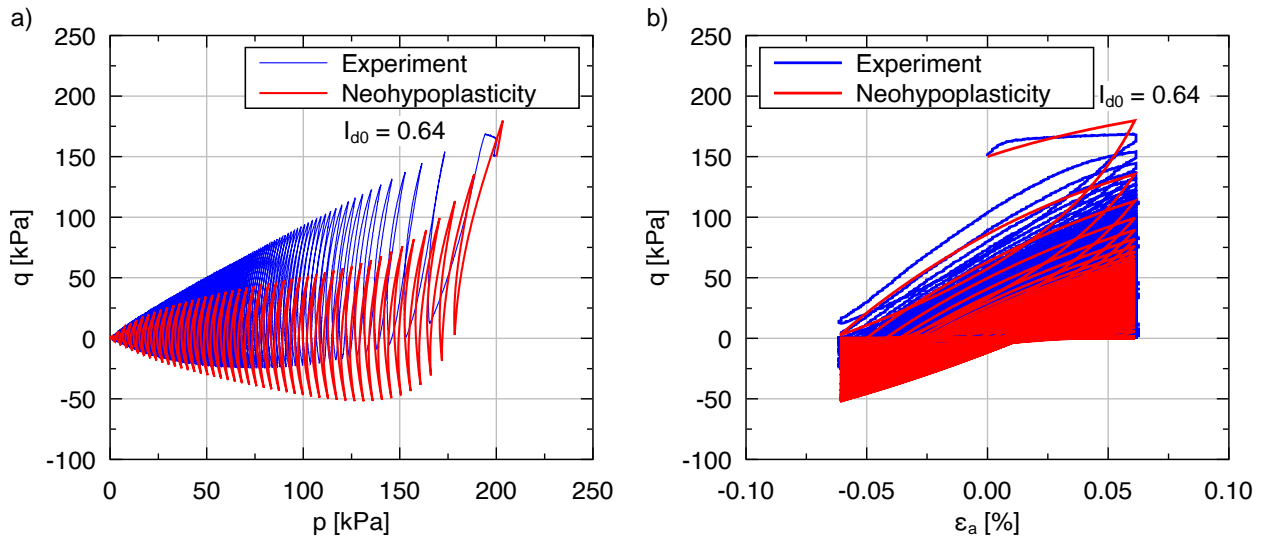

Figure 19: Anisotropic consolidated cyclic undrained triaxial test with a strain amplitude of $\Delta\varepsilon_1 = 6 \cdot 10^{-4}$: experimental results [36, 41] vs. calculations with NHP: a) stress path in $p - q$ diagram and b) deviator stress q as a function of axial strain ε_a.

4   Conclusion and Outlook

This paper presents a comprehensive and consistent description plus novel developments of the Neohypoplasticity (NHP). This includes an improvement of the evolution equation of the structural variable z and a simplified small strain stiffness approach by introducing a new tensorial state variable h^r. It is shown that the NHP can adequately reproduce the characteristic mechanical behaviour of sand. In particular, NHP overcomes some of the disadvantages of the Hypoplasticity (HP). Inadmissible tensile stress states are prevented and the dilatancy is better reproduced. The NHP was calibrated for Karlsruhe fine sand. Both monotonic and cyclic deformations were simulated and well reproduced. The state of the soil in NHP is described by four state variables:
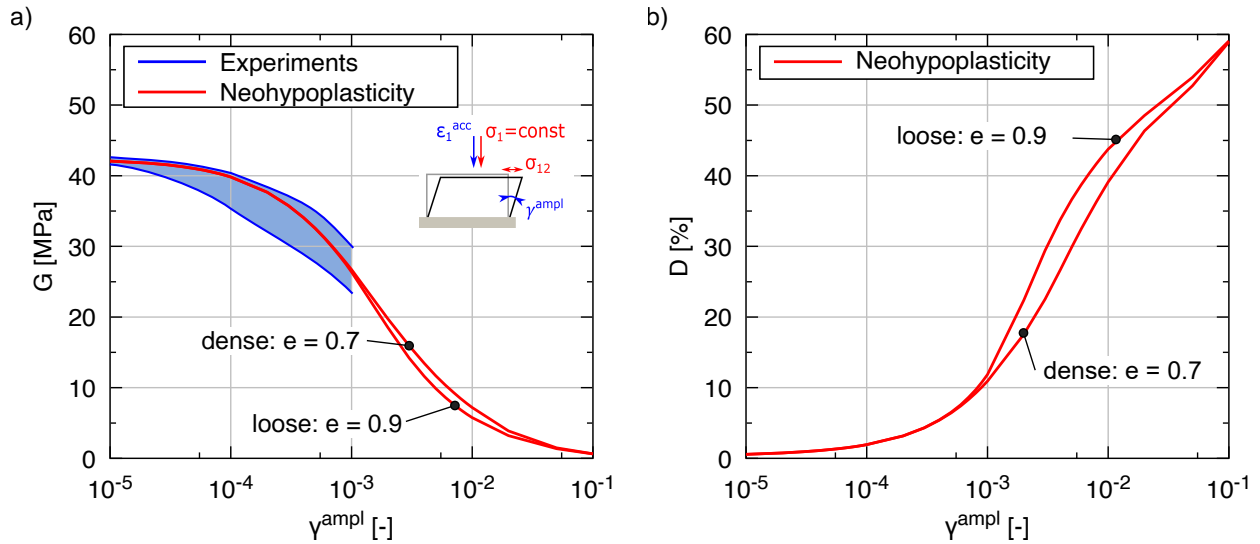
- stress σ
- void ratio e

18

Figure 20: Shear mudul G and damping ratio D as a function of shear strain amplitude γ^{ampl} in a drained simple shear test: simulation of NHP (red) and experimental results [36] (blue)

- structure variable $\boldsymbol{z}$

- last strain reversal $\boldsymbol{h}^r$

The essential components of NHP are the hyperelastic stiffness, the rotation of the elastic stiffness, the explicit formulation of the degree of nonlinearity, the hypoplastic flow rule and the small strain stiffness extension. The small strain stiffness approach leads at $Y = 1$ not to an overestimating of the shear strength. Further developments of NHP can be:

- The hypoplastic flow rule can be formulated as a function of stress and void ratio in order to describe more precisely the density dependence of the direction of plastic deformation.

- To represent the hysteric behaviour of soil at small strain amplitudes, a coupling using the Paraelasticity [24, 25, 32] is possible. This will replace the simplified approach in this paper. First approaches to this can be found in [20].

Users of the NHP may be discouraged by the large number of material constants. Nevertheless, the automatic calibration tools [14, 20] may erase the calibration of advanced constitutive models and promote applications of the NHP beyond the field of scientific research. Recommendations for the comparison and evaluation of constitutive models are given in the Appendix B. Finally, we would like to highlight, as already mentioned, that the user is recommended to calibrate only 10 of the 28 material parameters.

Appendix A

To calibrate A_z the shear strain ε_Q^z, which is approximately required to reach an isotropic stress state on the P-axis ($Q = 0$) from a stress state on the CSL, is estimated. The compliance component C_{QQ} from the hyperelastic stiffness is given by [22]

$$C_{QQ} = C_\alpha Q^2 R^{-2} + D_\alpha \tag{26}$$

with

$$D_\alpha = c(2 - n - \alpha) P^\alpha R^{-n-\alpha}. \tag{27}$$

We assume that the deviatoric stress Q does not influence the evolution of $\boldsymbol{z}$. This justifies the assumption of $Q = 0$ and the corresponding compliance component is obtained with $R = \sqrt{P^2 + Q^2} = P$:

$$C_{QQ} = c(2 - n - \alpha)P^{-n} \tag{28}$$

In accordance with the Mohr-Coulomb criterion, for $\varphi = 30°$ applies in the $P - Q$ space

$$-0.4041 = -\frac{2\sqrt{2}\sin\varphi}{3 + \sin\varphi} \leq \frac{Q}{P} = M \leq \frac{2\sqrt{2}\sin\varphi}{3 - \sin\varphi} = 0.5657 \tag{29}$$

The initial state is assumed to be a stress state with $M = 0.4$ and $Y = 1$ (extension zone, the sign is irrelevant). For the ratio of compliance in HP applies $C_{QQ}(Y = 1) = 1/2 \cdot C_{QQ}(Y = 0)$. The mean value $\overline{C}_{QQ} = 3/4 \cdot C_{QQ}$ is assumed for simplification. Within the current further development of NHP, the small strain stiffness was taken into account using a simplified approach, described in more detail in Section 2.8. The stiffness is increased using a factor k after a reversal of the loading direction. The decrease of k with the strain distance from the last strain reversal is described by the Equation (24). For simplification, the factor $\overline{k} = 0.7m_R$ is assumed as the average stiffness increase in the range of $0 < ||\varepsilon_{ij} - h_{ij}^r|| = d^r < 0.001$. This further reduces the applied compliance to $\overline{C}_{QQ} = 3/4 \cdot C_{QQ}/(0.7m_R)$. For the shear strain ε_Q^z we obtain:

$$\varepsilon_Q^z = Q \cdot \overline{C}_{QQ} = \frac{M \cdot P \cdot 3}{4} \cdot C_{QQ}/(0.7m_R) = 0.3 \cdot c(2 - n - \alpha)P^{-n+1}/(0.7m_R) \tag{30}$$

The objective of the calibration of A_z is to guarantee a $\boldsymbol{z}$ degradation starting from $z_{\max}$ at the strain ε_Q^z. For the given material parameters $\alpha_z = 0.01$, $n_z = 2$, $\beta_z = 0.1$ and $z_{\max} = 0.05$, the solution of the differential Equation (18) results in

$$A_z = 0.1/\varepsilon_Q^z = 0.198/(0.3 \cdot c(2 - n - \alpha)P^{-n+1}) \cdot 0.7m_R \tag{31}$$

For other combinations of material parameters, A_z has to be multiplied by a further scalar factor. An adjustment of these parameters by the user is explicitly not recommended. The function A_z thus takes into account the pressure dependence of the evolution of $\boldsymbol{z}$.

Appendix B

The authors would like to demonstrate the importance of an objective comparison of constitutive models. The monotonic drained triaxial tests shown in Figure 12 were simulated using given axial strain increments and the constraints $\sigma_{22} = \sigma_{33}$ and $\sigma_{12} = \sigma_{13} = \sigma_{23} = \varepsilon_{12} = \varepsilon_{13} = \varepsilon_{23}$. This can be called *mixed control*, since both strain and stress increments are specified. This results in the "nice looking" graphs shown in Figure 12. A different approach for recalculating the same experiments is to specify the whole strain path measured in the experiment. In this case, all six strain components are specified. With this *pure strain control*, the stress path is obtained as the result of the simulation. Results of simulations performed on the monotonic drained triaxial test with the densest sample from Figure 12 ($I_D = 0.85$) are shown in Figure 21. In addition to the calculations with NHP (red), simulations with HP+IS [23] (green) using the material parameter set from [36] are also shown. It becomes apparent that the simulation results now deviate significantly from the experimental data. The example shows that HP+IS even leads to a complete reduction in effective stresses. The comparatively smaller error in NHP is caused by a better representation of the dilatancy.

This example demonstrates that constitutive models should generally be tested and compared on the basis of objective criteria. A comparison of experimental and simulation data in terms of "nice looking" curves does not fulfil this objectivity. Further aspects on computer-aided calibration, benchmarking and check-up of constitutive models can be found in [20].
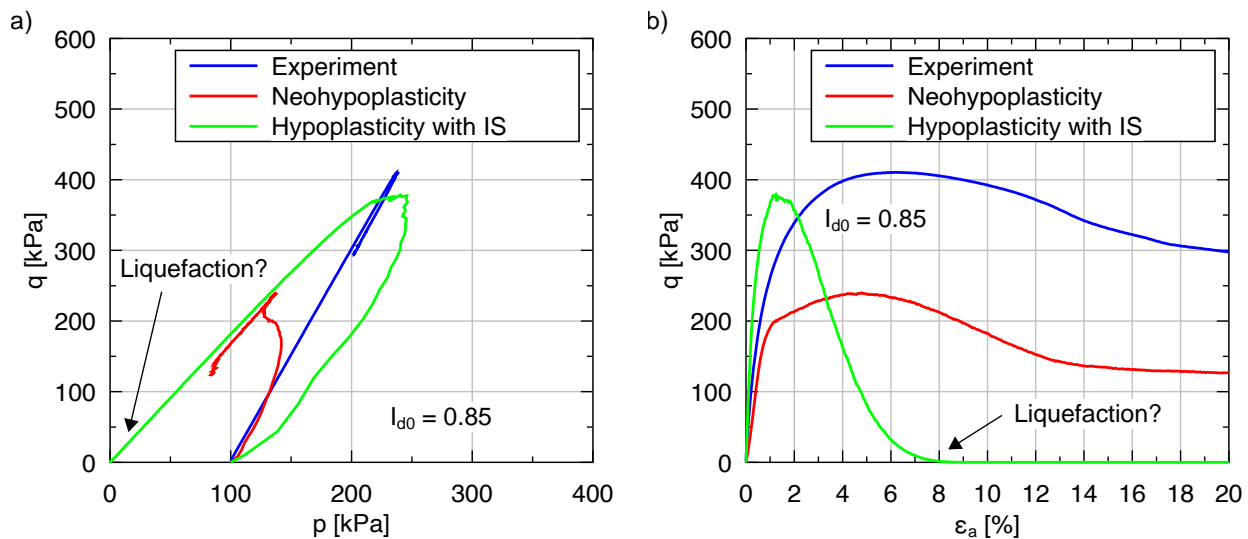
Figure 21: Monotonic drained triaxial test of a dense sample (the same as in Figure 12): Experimental data (blue curve) [36, 41] and simulation results of NHP (red) and HP+IS [23] (green) with a pure strain control.

References

[1] M. Arnold and I. Herle. Comparison of vibrocompaction methods by numerical simulations. *International Journal for Numerical and Analytical Methods in Geomechanics*, 33(16):1823–1838, 2009.

[2] E. Bauer. Calibration of a comprehensive hypoplastic model for granular materials. *Soils and Foundations*, 36(1):13–26, 1996.

[3] Y. F. Dafalias and M. T. Manzari. Simple plasticity sand model accounting for fabric change effects. *Journal of Engineering Mechanics*, 130(6):622–634, 2004.

[4] J. Duque, M. Yang, W. Fuentes, D. Mašín, and M. Taiebat. Characteristic limitations of advanced plasticity and hypoplasticity models for cyclic loading of sands. *Acta Geotechnica*, 17(6):2235–2257, 2022.

[5] W. Fuentes. *Contributions in mechanical modeling of fill materials*. Dissertation, Publications of the Institute of Soil Mechanics and Rock Mechanics, Karlsruhe Institute of Technology, Issue No. 179, 2014.

[6] C. E. Grandas Tavera, T. Triantafyllidis, and L. Knittel. A constitutive model with a historiotropic yield surface for sands. In *Recent Developments of Soil Mechanics and Geotechnics in Theory and Practice*, pages 13–43. Springer, Cham, 2020.

[7] G. Gudehus. A comparison of some constitutive laws for soils under radially symmetrical loading and unloading. In *Proceedings of the 3rd International Conference on Numerical Methods in Geomechanics, Aachen*, volume 4, pages 1309–1323. Balkema, 1979.

[8] G. Gudehus. A comprehensive constitutive equation for granular materials. *Soils and Foundations*, 36(1):1–12, 1996.

[9] I. Herle and G. Gudehus. Determination of parameters of a hypoplastic constitutive model from properties of grain assemblies. *Mechanics of Cohesive-frictional Materials*, 4(5):461–486, 1999.

[10] L. Knittel, T. Wichtmann, A. Niemunis, G. Huber, E. Espino, and T. Triantafyllidis. Pure elastic stiffness of sand represented by response envelopes derived from cyclic triaxial tests with local strain measurements. *Acta Geotechnica*, 15(8):2075–2088, 2020.

[11] D. Kolymbas. An outline of hypoplasticity. *Archive of Applied Mechanics*, 61(3):143–151, 1991.

[12] D. Kolymbas and G. Medicus. Genealogy of hypoplasticity and barodesy. *International Journal for Numerical and Analytical Methods in Geomechanics*, 40(18):2532–2550, 2016.

[13] I. Loges and A. Niemunis. Neohypoplasticity - estimation of small strain stiffness. In T. Triantafyllidis, editor, *Holistic Simulation of Geotechnical Installation Processes*, volume 77 of *Lecture Notes in Applied and Computational Mechanics*, pages 163–180. Springer International Publishing, Cham, 2015.

[14] J. Machaček, P. Staubach, C. E. Grandas-Tavera, T. Wichtmann, and H. Zachert. On the automatic parameter calibration of a hypoplastic soil model. *Acta Geotechnica*, 17(11):5253–5273, 2022.

[15] J. Machaček, P. Staubach, M. Tafili, H. Zachert, and T. Wichtmann. Investigation of three sophisticated constitutive soil models: From numerical formulations to element tests and the analysis of vibratory pile driving tests. *Computers and Geotechnics*, 138:104276, 2021.

[16] D. Mašín. *Modelling of Soil Behaviour with Hypoplasticity*. Springer International Publishing, Cham, 2019.

[17] H. Matsuoka and T. Nakai. Stress-strain relationship of soil based on the smp, constitutive equations of soils. In S. Murayama and A. N. Schofield, editors, *Speciality Session 9*, 1977.

[18] S. Nagula, M. Nguyen, J. Grabe, J. Kardel, and T. Bahl. Field measurements and numerical analysis of vibroflotation of sand. *Géotechnique*, 72(10):882–898, 2022.

[19] A. Niemunis. *Extended hypoplastic models for soils*. Habilitation, Publications of the Institut für Grundbau und Bodenmechanik, Ruhr-Universität Bochum, Issue No. 34, 2003.

[20] A. Niemunis and C. E. Grandas Tavera. Computer aided calibration, benchmarking and check-up of constitutive models for soils. some conclusions for neohypoplasticity. In *Holistic Simulation of Geotechnical Installation Processes*, pages 168–192. Springer, Cham, 2017.

[21] A. Niemunis and C. E. Grandas Tavera. Essential concepts of neohypoplasticity. In Wei Wu, editor, *Desiderata Geotechnica*, Springer eBooks Engineering, pages 132–142. Springer, Cham, 2019.

[22] A. Niemunis, C. E. Grandas Tavera, and T. Wichtmann. Peak stress obliquity in drained and undrained sands. simulations with neohypoplasticity. In *Holistic Simulation of Geotechnical Installation Processes*, pages 85–114. Springer, Cham, 2016.

[23] A. Niemunis and I. Herle. Hypoplastic model for cohesionless soils with elastic strain range. *Mechanics of Cohesive-frictional Materials*, 2(4):279–299, 1997.

[24] A. Niemunis, L. F. Prada-Sarmiento, and C. E. Grandas Tavera. Extended paraelasticity and its application to a boundary value problem. *Acta Geotechnica*, 6(2):81–92, 2011.

[25] A. Niemunis, L. F. Prada-Sarmiento, and C. E. Grandas Tavera. Paraelasticity. *Acta Geotechnica*, 6(2):67–80, 2011.

[26] A. Niemunis, T. Wichtmann, and T. Triantafyllidis. A high-cycle accumulation model for sand. *Computers and Geotechnics*, 32(4):245–263, 2005.

[27] P. Norlyk, K. Sørensen, L. V. Andersen, K. K. Sørensen, and H. H. Stutz. Holistic simulation of a subsurface inflatable geotechnical energy storage system using fluid cavity elements. *Computers and Geotechnics*, 127:103722, 2020.

[28] V. A. Osinov. Wave-induced liquefaction of a saturated sand layer. *Continuum Mech. Thermodyn*, 12:325–339, 2000.

[29] V. A. Osinov. Large-strain dynamic cavity expansion in a granular material. *Journal of Engineering Mathematics*, 52(1-3):185–198, 2005.

[30] V. A. Osinov, S. Chrisopoulos, and T. Triantafyllidis. Numerical study of the deformation of saturated soil in the vicinity of a vibrating pile. *Acta Geotechnica*, 8(4):439–446, 2013.

[31] V. A. Osinov, S. Chrisopoulos, and T. Triantafyllidis. Numerical analysis of the tunnel-soil interaction caused by an explosion in the tunnel. *Soil Dynamics and Earthquake Engineering*, 122:318–326, 2019.

[32] L. F. Prada-Sarmiento. *Paraelastic description of small-strain soil behaviour*. Dissertation, Publications of the Institute of Soil Mechanics and Rock Mechanics, Karlsruhe Institute of Technology, Issue No. 173, 2011.

[33] P. Staubach, J. Machaček, and T. Wichtmann. Large-deformation analysis of pile installation with subsequent lateral loading: Sanisand vs. hypoplasticity. *Soil Dynamics and Earthquake Engineering*, 151:106964, 2021.

[34] A. S. Vesić. Analysis of ultimate loads of shallow foundations. *Journal of the Soil Mechanics and Foundations Division*, 99(1):45–73, 1973.

[35] P.-A. von Wolffersdorff. A hypoplastic relation for granular materials with a predefined limit state surface. *Mechanics of Cohesive-frictional Materials*, 1(3):251–271, 1996.

[36] T. Wichtmann. *Soil behaviour under cyclic loading - experimental observations, constitutive description and applications*. Habilitation, Publications of the Institute of Soil Mechanics and Rock Mechanics, Karlsruhe Institute of Technology, Issue No. 181, 2016.

[37] T. Wichtmann, W. Fuentes, and T. Triantafyllidis. Inspection of three sophisticated constitutive models based on monotonic and cyclic tests on fine sand: Hypoplasticity vs. sanisand vs. isa. *Soil Dynamics and Earthquake Engineering*, 124:172–183, 2019.

[38] T. Wichtmann, M. A. Navarrete Hernández, and T. Triantafyllidis. On the influence of a non-cohesive content of fines on the small strain stiffness of quartz sand. *Soil Dynamics and Earthquake Engineering*, 69(2):103–114, 2014.

[39] T. Wichtmann and T. Triantafyllidis. Influence of the grain size distribution curve of quartz sand on the small strain shear modulus gmax. *Journal of Geotechnical and Geoenvironmental Engineering, ASCE*, 135(10):1404–1418, 2009.

[40] T. Wichtmann and T. Triantafyllidis. Stiffness and damping of clean quartz sand with various grain size distribution curves. *Journal of Geotechnical and Geoenvironmental Engineering, ASCE*, 140(3), 2014.

[41] T. Wichtmann and T. Triantafyllidis. An experimental database for the development, calibration and verification of constitutive models for sand with focus to cyclic loading: part i—tests with monotonic loading and stress cycles. *Acta Geotechnica*, 11(4):739–761, 2016.

[42] T. Wichtmann and T. Triantafyllidis. An experimental database for the development, calibration and verification of constitutive models for sand with focus to cyclic loading: part ii—tests with strain cycles and combined loading. *Acta Geotechnica*, 11(4):763–774, 2016.

[43] M. Wotzlaw, D. Aubram, and F. Rackwitz. Numerical analysis of deep vibrocompaction at small and full scale. *Computers and Geotechnics*, 157:105321, 2023.

[44] W. Wu, E. Bauer, and D. Kolymbas. Hypoplastic constitutive model with critical state for granular materials. *Mechanics of Materials*, 23(1):45–69, 1996.